Received: 9 April 2020 | Revised: 30 July 2020 | Accepted: 2 August 2020

DOI: 10.1002/app.49826

ARTICLE

Applied Polymer SCIENCE WILEY

Development of layer-by-layer assembled thin coatings on aluminium alloy AA2024-T3 for high resolution studies of local corrosion processes

Ahed Almalla[1,2] | **Andreas Hertwig**[1] | **Daniel Fischer**[1] | **Ozlem Ozcan**[1] | **Julia Witt**[1]

[1]Bundesanstalt für Materialforschung und -prüfung (BAM), Berlin, Germany

[2]Freie Universität Berlin, Berlin, Germany

Correspondence
Julia Witt, Bundesanstalt für Materialforschung und -prüfung (BAM), Unter den Eichen 87, Berlin 12205, Germany.
Email: julia.witt@bam.de

Abstract

The aim of this study is to develop nanometer-thin epoxy-based films on aluminium alloy AA2024-T3 as a model coating system for high resolution corrosion studies. Spin coating was used for the layer-by-layer (LbL) deposition of poly-(ethylenimine) (PEI) and poly([o-cresyl glycidyl ether]-co-formaldehyde) (CNER) bilayers. The film chemistry and the cross-linking process were characterized by means of Fourier-transform infrared spectroscopy (FTIR). Ellipsometric data confirmed the linear increase of film thickness. The potentiodynamic polarization and electrochemical impedance spectroscopy (EIS) results indicate the improvement of the film barrier properties with increasing film thickness. Mapping of the topography and the volta potential was performed by means of scanning Kelvin probe force microscopy (SKPFM). The results indicate the presence of a homogeneous film structure, while the intermetallic phases can still be identified below the coating. The SKPFM analysis confirmed that the model films are suitable for investigation of corrosion processes at the coating/metal interface.

KEYWORDS

coatings, electrochemistry, microscopy, resins, spectroscopy

1 | INTRODUCTION

Epoxy resins are widely used in several industrial areas as protective coatings due to its low cost and excellent corrosion resistance performance. Frequently used epoxy curing agents include amines, which allow a high cross-link density of the coating system at a low curing temperature. Understanding how these coatings provide corrosion protection and how the protection may be compromised at the coating/metal interface is of particular interest, but the preparation of thin and uniform films is not a trivial task as epoxy coatings show a high tendency to undergo phase separation and pore formation.[1]

The aluminium alloy AA2024-T3 (92.5% Al, 4.5% Cu, 1.5% Mn, and 0.5% Mg) is extensively used in aerospace applications due to its high strength and low weight. The microstructural heterogeneity improves the mechanical properties,[2] however the presence of intermetallic particles (IMPs) results in a higher susceptibility to galvanic corrosion.[3–5] The implication of IMPs on

the local corrosion behavior of AA2024-T3 and especially their contribution to the initiation of pitting and intergranular corrosion in aqueous solutions containing aggressive chemical species such as chloride is well documented.[6–9] However, the complex structure and composition of the IMPs are the main reasons representing the difficulties in understanding the very initial corrosion mechanisms.

Several authors reported the application of in situ techniques aiming at a better mechanistic understanding of the localized corrosion activity on AA2024-T3 at the nanometer scale.[10–12] Atomic force microscopy (AFM) has been shown to be a powerful tool to characterize morphological surface changes associated with the initial stages of corrosion. Operated in the scanning Kelvin probe microscopy (SKPFM) mode AFM can deliver the Volta Potential distribution of the investigated surface, enabling the identification of IMPs.[10–12] Another strength of the SKPFM technique is the ability to access information at buried polymer/metal interfaces which is useful to visualize corrosion induced delamination processes at polymer coated metal surfaces.[13–14]

An ideal condition for SKPFM investigations is given by a smooth surface and film thickness lower than ~500 nm guaranteeing a high resolution and a potential response free of topography induced artifacts.[15–16] However, the synthesis of classical two-component epoxy-amine thin films is not straightforward in this thickness regime, due to the immediate cross-linking and the resulting increase in viscosity. Thus, the development of thin model layers mimicking the epoxy-amine chemistry is necessary to create an appropriate system for the investigation of interfacial corrosion and delamination processes. Qureshi et al.[17] demonstrated a covalent layer-by-layer (LbL) dip-coating method for the fabrication of mechanically robust nanoscale films consisting of the oligomeric Novolac® epoxy resin poly[(o-cresyl glycidyl ether)-co-formaldehyde] (CNER) and poly(ethyleneimine) (PEI). They have reported that the film thickness for a CNER-PEI bilayer increased both with increasing polymer concentration and with increasing adsorption times up to approximately 6 nm.

In this study, we extend this approach of film fabrication by utilizing the spin coating method for the deposition of thin and uniform films composed of CNER and PEI on AA2024-T3 after optimization of the deposition procedure and solvent selection to increase the efficiency of film synthesis. SKPFM results confirm the applicability of the epoxy coatings as a model system for studies of the corrosion and delamination behavior at the coating/metal interface. Complementary electrochemical and spectroscopic studies were used for the investigation of film build-up process and its corrosion protection properties.

2 | EXPERIMENTAL

2.1 | Sample preparation

AA2024-T3 (nominal composition: 93.5% Al, 4.5% Cu, 1.5% Mg, and 0.5% Mn; Goodfellow, Friedberg, Germany) coupons of dimensions 20 mm × 20 mm × 1.6 mm were cut from sheet material and wet grounded using silicon carbide papers (ATM GmbH, Germany) up to 4000 grit and further polished with 3 μm and 1 μm diamond monocrystalline paste (ATM GmbH, Germany) subsequently. After each polishing step, the samples were rinsed with deionized water (0.055 μS/cm, Evoqua, USA). Finally, the coupons were cleaned in an ultrasonic bath in ethanol and dried in an oil-free compressed air stream.

CNER (Poly[(o-cresyl glycidyl ether)-co-formaldehyde], trade name Cresol Novolac epoxy resin, average M_n ~ 1080 g/mol; Sigma Aldrich, Steinheim, Germany) was dissolved in chloroform and PEI (branched poly(ethylenimine), average M_w ~ 25,000 g/mol; Sigma Aldrich, Steinheim, Germany) solution was prepared in ethanol, both with a total concentration of 0.2% (w/w). The deposition of the CNER and PEI layers was performed under ambient conditions using SPIN150 spin coater (APT GmbH, Germany). Each bilayer consists of one PEI layer and one CNER layer, while PEI is being the first layer which is contact with AA2024-T3. For the spin coating process, a 400 μl solution was placed on the sample surface. The sample was accelerated with 1000 rpm/s^2 to the desired rotation speed of 3000 rpm where it rotates at constant rpm for 30 s. The initial optimization of film build-up was performed by synthesizing 1 bilayer (BL) films using different solvent combinations listed in Table 1. For optimization of the curing time, ethanol and chloroform have been selected as solvents for PEI and CNER, respectively based on the film homogeneity assessed by means of AFM topography analysis. Thin films consisting of one, two, four and eight BLs were prepared and investigated. Three sets of samples were prepared on AA2024-T3 substrates with curing at 80°C for 30, 10 or 1 min after each BL. Bare AA2024-T3 samples were denoted as AA, while coated samples were specified as $(CNER/PEI)_n$/AA with n = 1, 2, 4 and 8 for the BL number.

2.2 | Sample characterization

Fourier-transform infrared spectroscopy (FTIR) spectra were recorded in external reflection mode with a Nicolet

TABLE 1 Tested solvent combinations for deposition of the CNER and PEI layers

	(a)	(b)	(c)	(d)	(e)	(f)
PEI	Ethanol	Chloroform	Ethanol	Chloroform	Ethanol	Chloroform
CNER	Acetone	Chloroform	THF	Acetone	Chloroform	THF

Abbreviations: CNER, poly([o-cresyl glycidyl ether]-co-formaldehyde); PEI, poly-(ethylenimine); OCP, open circuit potential.

8700 FT-IR spectrometer (Thermo Fisher Scientific, USA) equipped with VeeMAX III specular reflection accessory (Pike Technologies, USA). The spectra were collected at 80° incidence angle using a a liquid nitrogen cooled mercury cadmium telluride (MCT) detector, with a resolution of 4 cm^{-1} by averaging over 512 single scans to achieve spectra with a high signal to noise ratio. Data acquisition and spectra processing was performed with the OMNIC software (Thermo Fisher Scientific, USA).

Scanning Kelvin probe force microscopy (SKPFM) measurements were performed under ambient conditions with a NanoWizard 4 (JPK Instruments, Berlin, Germany) operating with a resolution of 512 × 512 pixels. At the first scan, the intermittent mode was used to measure the topography, whereas at the second scan the tip was lifted by a predefined height of 50 nm and an AC voltage of 1 V was applied to the tip to determine the surface potential following the topography profile. The AFM and SKPFM images were collected at a scan frequency of 0.5–1.0 Hz using silicon cantilevers with a conductive Cr/Pt-coating (Tap300-G: nominal spring constant of 40 N m^{-1} or, MULTI75E-G-50: nominal spring constant of 3 N m^{-1}, (Budget Sensors, Canada, USA) As no absolute reference was used in SKPFM analysis, the reported values are potential differences. The software JPK Data Processing Suite 6.1.88 was used for offline analysis of the topography and the film thickness. Image flattening was performed with the first order least-square polynomial function, which removes tilt and the vertical z-offset between line scans. The surface roughness values are given as the arithmetic average of the roughness profile (R_a) in a total area of 50 μm × 50 μm.

The determination of the film thickness was carried out by means of ellipsometry using M-2000UI ellipsometer (J.A. Woollam Co., Lincoln, Nebraska, USA). All measurements were performed in a spectral range of 192–1683 nm with a deuterium/halogen light source and incidence angles between 55°-75° using a step size of 5°. The results were analyzed using the C-EASE (version 6.3).

2.3 | Electrochemical studies

Potentiodynamic polarization measurements and electrochemical impedance spectroscopy (EIS) were performed at room temperature using Gamry Reference 600+ potentiostat (Gamry Instruments, USA) and the Gamry Framework data acquisition software (version 7.03). The experiments were conducted in an electrochemical cell specified by a working area of 0.5 cm^2. Bare and coated AA2024-T3 samples were used as the working electrode. An Au-wire and an Ag/AgCl/3 M NaCl electrode (C3 Prozessanalytik, Germany) served as counter and reference electrodes, respectively. The potentials were referred to the used reference electrode. Prior to each measurement, the open circuit potential (OCP) was measured for 6000 sec to reach equilibrium conditions. All experiments were performed in a 0.1 M $NaClO_4$ (PanReac AppliChem IWT Reagents; Darmstadt, Germany) electrolyte solutions prepared with deionized water (0.055 μS/cm, Evoqua, USA).

3 | RESULTS AND DISCUSSION

3.1 | Effect of solvent selection on film morphology

The initial selection of solvents for spin coating of PEI and CNER layers was performed on AA2024-T3 substrates to optimize the deposition process and study the effects of solvent combinations on the film morphology. The tested solvent combinations are listed in Table 1. Using water as solvent for PEI was deliberately excluded from the test matrix as contact with an aqueous solution may modify the surface chemistry of aluminium alloy in the investigations at further stages of the project. Moreover, rest water in the PEI film is expected to affect the CNER deposition negatively. Thus, organic solvents with different dielectric constants were tested for the deposition of PEI and CNER films as listed in Table 1. For PEI ethanol and chloroform were selected as a polar protic and a non-polar solvent, respectively. In case of CNER, polar aprotic acetone and THF as well as non-polar chloroform were tested as solvents.

The morphology of the one bilayer films was investigated by means of AFM topography analysis. All three bilayer films prepared using chloroform as solvent for PEI deposition (Figure 1(b),(d),(f)) have shown formation of globular agglomerates. Similar results were obtained with PEI[ethanol]/CNER[THF] (Figure 1(c). When acetone was used as the solvent for CNER deposition, the

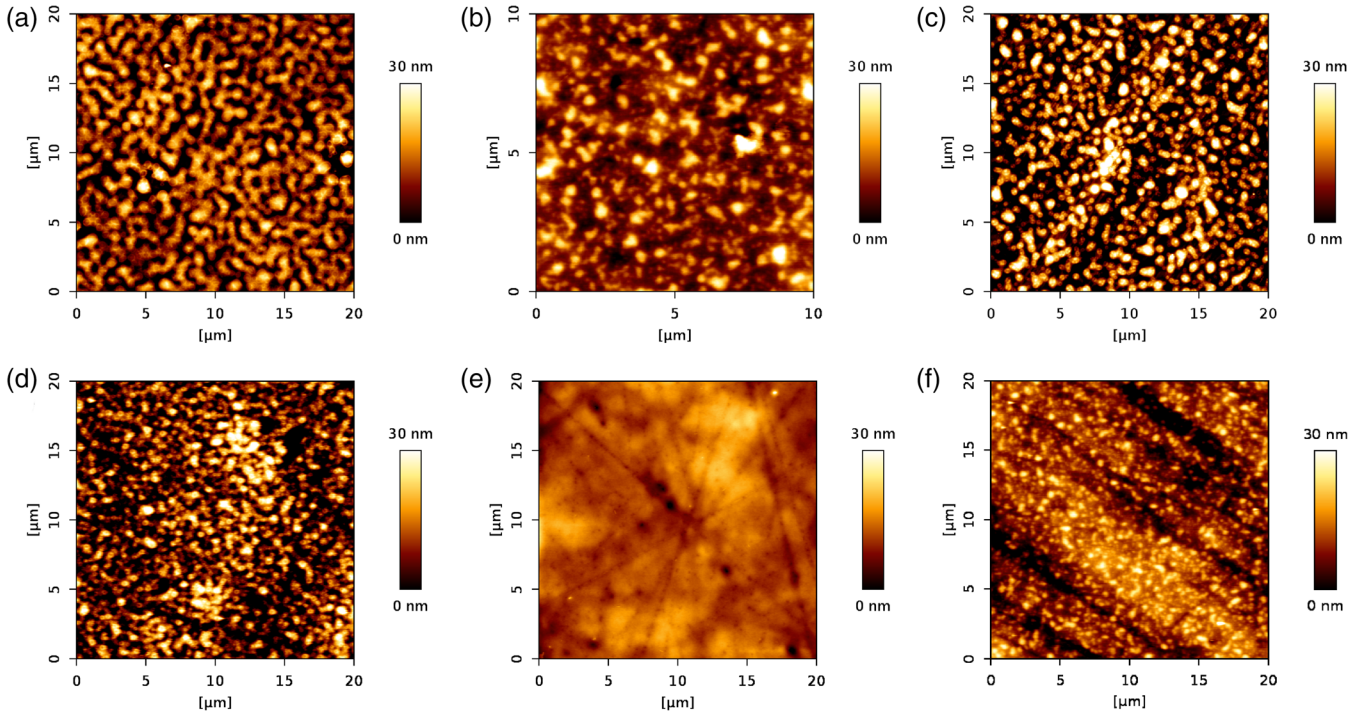

FIGURE 1 AFM images of $(CNER/PEI)_1/AA$ using different solvent combinations: (a) PEI(ethanol)/CNER(acetone), (b) PEI(chloroform)/CNER(chloroform), (c) PEI(ethanol)/CNER(THF), (d) PEI(chloroform)/CNER(acetone), (e) PEI(ethanol)/CNER (chloroform), and (f) PEI(chloroform)/CNER(THF). The images were recorded in the intermittent mode using a Multi75 tip with a nominal force constant of 3 N m^{-1}. AFM, atomic force microscopy; CNER, poly([o-cresyl glycidyl ether]-co-formaldehyde); FTIR, Fourier-transform infrared spectroscopy; PEI, poly-(ethylenimine) [Color figure can be viewed at wileyonlinelibrary.com]

high polarity and protic nature of ethanol resulted in a globular, incomplete film deposition with high surface roughness (Figure 1(a)). Qureshi et al. used a mixture of ethanol and acetone and achieved homogeneous and smooth ultrathin $(CNER/PEI)_n$ multilayer films on silicon wafer substrates. These films were prepared by dip coating while the film thickness for a BL increased up to approximately 6 nm in one pass. One explanation for the different results might be that the epoxy films prepared by spin coating are much thicker and the second one is that the used AA substrates can have a different effect on the deposition behavior than the silicon surface. Due to the excellent homogeneity and low roughness PEI[ethanol]/CNER[chloroform] (Figure 1(e)) was selected for further studies on AA2024T3 substrates.

3.2 | Analysis of the film chemistry and thickness

FTIR spectra of the coatings were analyzed to identify the molecular structure of the BL films before and after curing and to confirm the growth of subsequent layers. FTIR spectra of freshly prepared and cured 1 BL films are presented in Figure 1. The FTIR spectra of the freshly prepared and cured sample reveal characteristic IR absorption modes for PEI and CNER. The observed modes at 3500–3300 cm^{-1} have a complex composition and might correspond to the N-H stretching vibrations of secondary amines in PEI, as well as to the -OH stretching vibrations of aluminium hydroxide formed on the aluminium surface and to water which might be trapped within the polymer film.[18] The deformation mode of primary and secondary amines can be observed at the wavenumber of 1585 and 1450 cm^{-1}.[19] The weak IR mode at 3005 cm^{-1} arises due to the sp^2 C-H stretching vibration on the aromatic carbon of CNER, while the C=C stretches of the aromatic ring appear in pairs at a wavenumber of 1601 and 1480 cm^{-1}. The absorption band at 1506 cm^{-1} is due to the C-C stretch in the aromatic ring.[20] The CH_2-O-CH bending mode of the oxirane group appears at 913 cm^{-1}.[20–21] The spectra show in the fingerprint region between 980–1250 cm^{-1} the stretching vibrations of the ether groups[20] and between 2800–2930 cm^{-1} the C-H stretching vibrations.[19] The band observed at 855 cm^{-1} could be assigned to the stretching vibrations of the oxirane ring.[20]

The comparison of the spectra before and after curing shows that the absorption modes at 3056 cm^{-1} and 3000 cm^{-1}, assigned to the stretching vibrations of the -CH and $-CH_2$ groups of the oxirane ring, disappeared after the heat treatment of the BLs at 80°C for 10 min

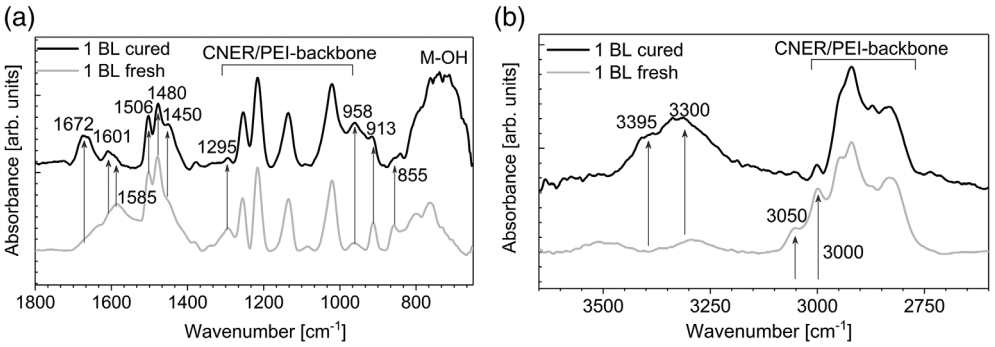

FIGURE 2 FTIR spectra of $(CNER/PEI)_1/AA$ before (gray line) and after (black line) curing in the spectral region of (a) 980–1250 cm^{-1} and (b) 2800–2930 cm^{-1}. CNER, poly ([o-cresyl glycidyl ether]-co-formaldehyde); FTIR, Fourier-transform infrared spectroscopy; PEI, poly-(ethylenimine)

(Figure 2(b)) confirming the opening of the oxirane ring and the cross-linking between CNER and the PEI the hardener.[21] The deformation mode of primary and secondary amines at 1585 and 1450 cm^{-1} show an opposite trend, where the intensity of the former is decreasing while the latter becomes more pronounced, which could further confirm the cross-linking reaction. The stretching vibrations of the ether groups between 980–1250 cm^{-1} and the C-H stretching vibrations between 2800–2930 cm^{-1} are not changing during the curing process indicating in the spectra as the CNER/PEI backbone. Similarly, the C-C and C=C stretching vibrations observed at 1480 and 1506 cm^{-1} as well as the CH_2-O-CH bending mode of the oxirane group at 913 cm^{-1} are not affected by the curing process significantly. The intensity of the peak assigned to the stretching vibrations of the oxirane ring at 855 cm^{-1} is slightly decreasing along with the emergence of the Al–O valence band at about 958 cm^{-1},[22] which could be explained with the thermal aging of the thin oxide/hydroxide layer. As seen in Figure 2(a),(b), the intensity of the broad peaks assigned to water/hydroxyl groups and -NH_2 between 3250–3450 cm^{-1}[23] is increased after the curing process. The increase of hydroxyl-vibrations might be explained by the trapping of the cross-linking-induced water in the film structure, as the thermal treatment is performed under 100 °C. Another indication of this phenomenon is the increase of the peak intensities below 800 cm^{-1}, which are assigned to the formation of metal hydroxides at the coating/metal interface.[24] The appearance of the peak at 1672 cm^{-1} can be attributed to scissoring vibrations of water molecules[22] and the interaction of the amide band with the stretching C=O vibrations.[19]

To establish an efficient coating process, the curing procedure was optimized by testing samples prepared with curing as last step and with intermediate curing after each bilayer for different durations. The fingerprint regions of the FTIR spectra of $(CNER/PEI)_1/AA$ and $(CNER/PEI)_4/AA$ prepared with curing as last step and with intermediate curing are presented in Figure 3. It can clearly be seen that the continuous deposition of the PEI/CNER bilayer system with subsequent curing as the last step did not lead to a continuous layer growth, which indicates that the not-cross-linked wet films can be removed from the surface during the deposition of the consecutive layers. This can be explained by the usage of organic solvents leading to the suppression of the electrostatic interactions between the bilayer components. As seen in Figure 3, the FTIR spectra of the 4BL films cured after the deposition of each bilayer reveal characteristic IR absorption modes for PEI and CNER as well as a proportional increase of intensities of the respective peaks in comparison to the 1BL coating.

For the optimization of the curing time, intermediate curing was performed for 1, 10 and 30 minutes between the deposition of bilayers for samples consisting of 1, 2, 4 and 8 bilayers. The determination of layer thicknesses and the correlation between curing time and the number of BLs was conducted by means of ellipsometry. The calculated thickness values are plotted in Figure 4 as a function of the curing time (30, 10 or 1 min) of each BL vs. the BL number and summarized in Table 2. Independent of the curing duration, the first BL has almost the same thickness of approximately 30 nm. However, for the curing duration of 1 min a slow increase in film thickness was observed (52 nm after eight BLs). The explanation could be that a short heat treatment may cause an insufficient cross-linking of the BLs resulting in a partial removal of the underlaying BLs with further deposition cycles, as observed with samples cured as the last step. This assumption was confirmed, since a linear growth of the film thickness was achieved at curing durations of 10 (210 nm after eight BLs) and 30 min (232 nm after eight BLs). Due to a small difference in the resulted layer thickness, only samples prepared with 10 min intermediate curing were considered in the reported AFM and electrochemistry studies.

3.3 | SKPFM analysis of the model films

The SKPFM was used to characterize the topography of the coatings and the Volta potential at the buried

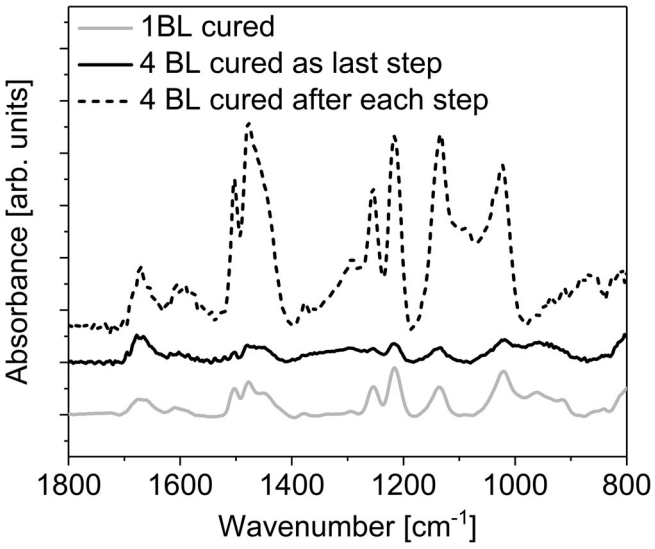

FIGURE 3 Comparison of the FTIR spectra of $(CNER/PEI)_1$/AA and $(CNER/PEI)_4$/AA prepared by curing as last step and with intermediate curing after each step. CNER, poly([o-cresyl glycidyl ether]-co-formaldehyde); FTIR, Fourier-transform infrared spectroscopy; PEI, poly-(ethylenimine)

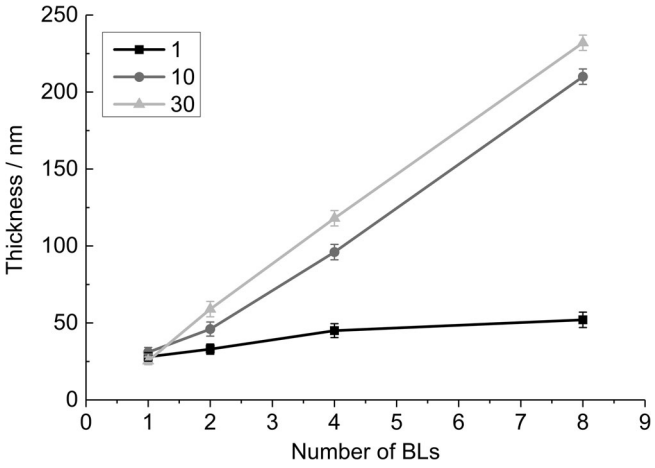

FIGURE 4 Thickness of the films determined by means of ellipsometry for different intermediate curing durations. CNER, poly([o-cresyl glycidyl ether]-co-formaldehyde); PEI, poly-(ethylenimine)

interface between the nanometer-thin coating and AA surface. The topography (top) and the potential map (bottom) acquired on a freshly polished AA surface is presented in Figure 5(a). The topography of the bare AA surface is dominated by polishing scratches with depths less than 30 nm. The IMPs protrude from the polished surface, since they possess a higher hardness and consequentially a lower polishing rate relative to the aluminium matrix. The topographical images reveal a smooth and homogeneous film structure (Figure 5(b)-(d)). Although, the polishing scratches are still present at the surface of $(CNER/PEI)_1$/AA, the average roughness decreases (R_a = 1.89 nm) in comparison to the AA surface (R_a = 3.71 nm). Further measurements indicate that the surface roughness of $(CNER/PEI)_4$/AA (R_a = 1.15 nm) and $(CNER/PEI)_8$/AA (R_a = 0.34 nm) decreases with the number of deposited BLs, which is also clearly visible as the polishing streaks disappear with thicker layers. In order to provide a better comparability of roughness values, a total area of 50 μm × 50 μm free of large IMPs was chosen for the determination.

The Volta potential map identifies the location of IMPs in AA, which show a clear potential contrast relative to the matrix (Figure 5(a), bottom). Fe-containing particles (Figure 5(a), particle A) are more noble than the surrounding Al matrix. After the deposition of the thin films it is still possible to identify the location and potential differences of the IMPs. In the topography (Figure 5 (b)-(d)), the IMPs under the polymer layer remain still recognizable as higher surface features, making the multilayer coatings with precisely adjustable thickness an ideal model system for the investigation of localized corrosion processes.

3.4 | Electrochemical analysis of the model coatings

For application as a model coating the PEI/CNER bilayer thin films were characterized in terms of their corrosion properties by means of electrochemical techniques. The potentiodynamic polarization method and the EIS were used to characterize the corrosion performance of the coated aluminium alloy substrates depending on the layer thickness. Representative potentiodynamic polarization (Tafel) plots recorded on AA in comparison to $(CNER/PEI)_1$/AA, $(CNER/PEI)_4$/AA and $(CNER/PEI)_8$/AA are presented in Figure 6 with the E_{pit}, E_{corr} values summarized in Table 3.

The Tafel analysis indicates a small drop of the corrosion current after the deposition of the first BL, while the current continues to decrease with the increasing BL number indicating an improvement of the corrosion protection properties. In general, this behavior is accompanied by a positive shift of the corrosion potential E_{corr}. However, instead a potential shift in the negative direction was observed as the BL number increases. This behavior was reported with alloys containing magnesium,[25] aluminium,[26] aluminium alloys[27] and ferrous materials.[28] No significant changes were observed in the cathodic branch of the Tafel plot for 1 BL and 4 BL samples, indicating that the corrosion protection effect is based on the suppression of anodic

TABLE 2 Film thicknesses as a function of the number of BLs and the intermediate curing duration (30, 10 or 1 min)

	Film thickness (nm)			
Time (min)	**$(CNER/PEI)_1/AA$**	**$(CNER/PEI)_2/AA$**	**$(CNER/PEI)_4/AA$**	**$(CNER/PEI)_8/AA$**
1	28	33	45	52
10	31	46	96	210
30	30	59	118	232

Abbreviations: BLs, bi-layers; CNER, poly([o-cresyl glycidyl ether]-co-formaldehyde); PEI, poly-(ethylenimine).

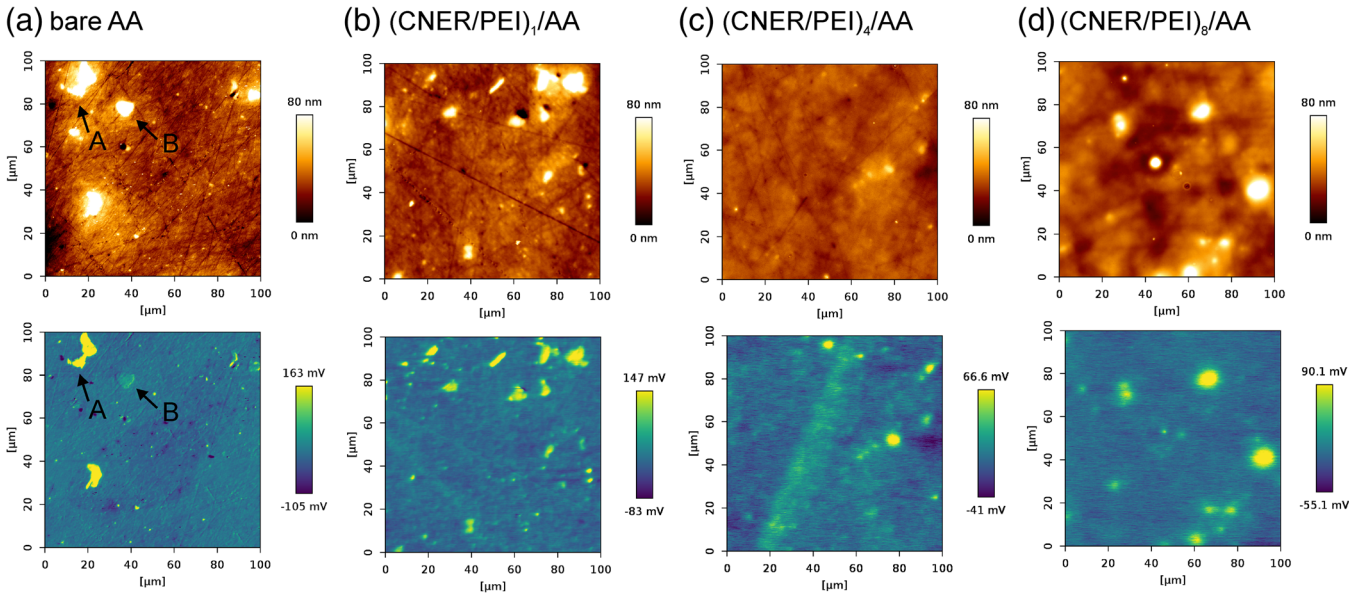

FIGURE 5 SKPFM topography (top) and Volta potential maps (bottom) of (a) bare AA, (b) $(CNER/PEI)_1/AA$, (c) $(CNER/PEI)_4/AA$, and (d) $(CNER/PEI)_8/AA$ recorded in the intermittent mode using a Tap300 tip with a nominal force constant of 40 N m^{-1}. The Volta potential map identifies the location of intermetallic Fe- (a) and Mg-containing (b) particles. CNER, poly([o-cresyl glycidyl ether]-co-formaldehyde); PEI, poly-(ethylenimine); SKPFM, scanning Kelvin probe microscopy [Color figure can be viewed at wileyonlinelibrary.com]

TABLE 3 Corrosion parameters obtained from the Tafel plots

Sample	**E_{corr} / V (vs. OCP)**	**E_{pit} / V (vs. OCP)**	**Δ_{pass}: E_{pit} - E_{corr} / V (vs. OCP)**
AA	−0.56	−0.46	0.10
$(PEI/CNER)_1/AA$	−0.61	−0.40	0.21
$(PEI/CNER)_4/AA$	−0.73	−0.29	0.44
$(PEI/CNER)_8/AA$	−0.87	−0.20	0.67

Abbreviations: CNER, poly([o-cresyl glycidyl ether]-co-formaldehyde); PEI, poly-(ethylenimine); OCP, open circuit potential.

metal dissolution resulting in a negative shift of the free corrosion potential. For the 8 BL films, the cathodic current densities have shown a half-fold decrease indicating that the diffusion of water is also hindered by the coating. The most significant effect was that thicker layers exhibit increasingly wider potential intervals free of pitting. The calculated values for the pitting free window Δ_{pass} increased from 0.21 V for 1BL to 0.67 V for 8 BL films.

To investigate the barrier properties of the model films, EIS measurements were performed. The resulting Bode Plots are presented in Figure 7(a),(b). The increase of the low frequency impedance and the appearance of the capacitance at ~5 kHz indicates that the barrier properties are improving with increasing film thickness. As the second time constant is only visible for 8 BL films, an equivalent circuit modeling with the classical paint model did not lead to an artifact-free identification of the

individual components. Therefore, for a qualitative analysis of the impedance response, the real and imaginary components of the impedance presented in Figure 7(c), (d) have been examined.

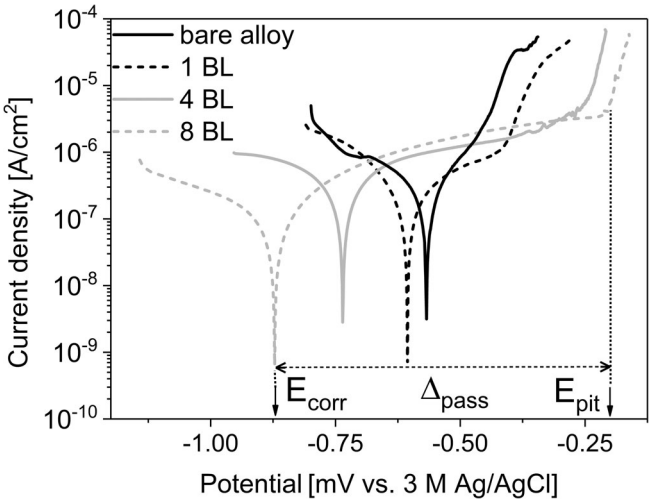

FIGURE 6 Tafel plots recorded in a 0.1 M $NaClO_4$ electrolyte solution at a scan rate of 1 mV s^{-1} on AA, $(CNER/PEI)_1/AA$, $(CNER/PEI)_4/AA$, and $(CNER/PEI)_8/AA$. The corrosion E_{corr} and pitting E_{pit} potential are indicated in the graph for the 8BL system as an example. CNER, poly([o-cresyl glycidyl ether]-co-formaldehyde); PEI, poly-(ethylenimine)

In the real component of the measured impedance presented in Figure 7(c) it can be clearly seen that resistive behavior at high frequencies was only observed with the 8 BL system. The 1 BL and 4 BL samples show an increase of low frequency resistive response, which can be attributed to the charge transfer resistance. According to the equivalent circuit analogy, the current will flow through the path of the lowest resistance, thus more current will pass via the capacitor if the coating resistance in the parallel configuration is higher. The selection of the path will also depend on the frequency of the AC perturbation signal.[29] As seen in Figure 7(d), the imaginary component of the impedance of the 8 BL system at 10 kHz is one order of magnitude higher than the values of 1 BL and 4 BL samples. At this frequency the overall impedance response of the 8 BL system is the result of the superposition of the electrolyte resistance and the coating capacitance. Therefore, only a minor decrease in the phase was observed. Interpreted together with the potentiodynamic polarization results, the EIS data indicate that the investigated bilayer films cannot fully prevent water ingress to the interface. However, with increasing film thickness, the model coatings can retard the diffusion of water. This also supports the observation that the cathodic corrosion processes like oxygen reduction are not suppressed by the presence of the 1 BL and 4 BL films and a decrease of

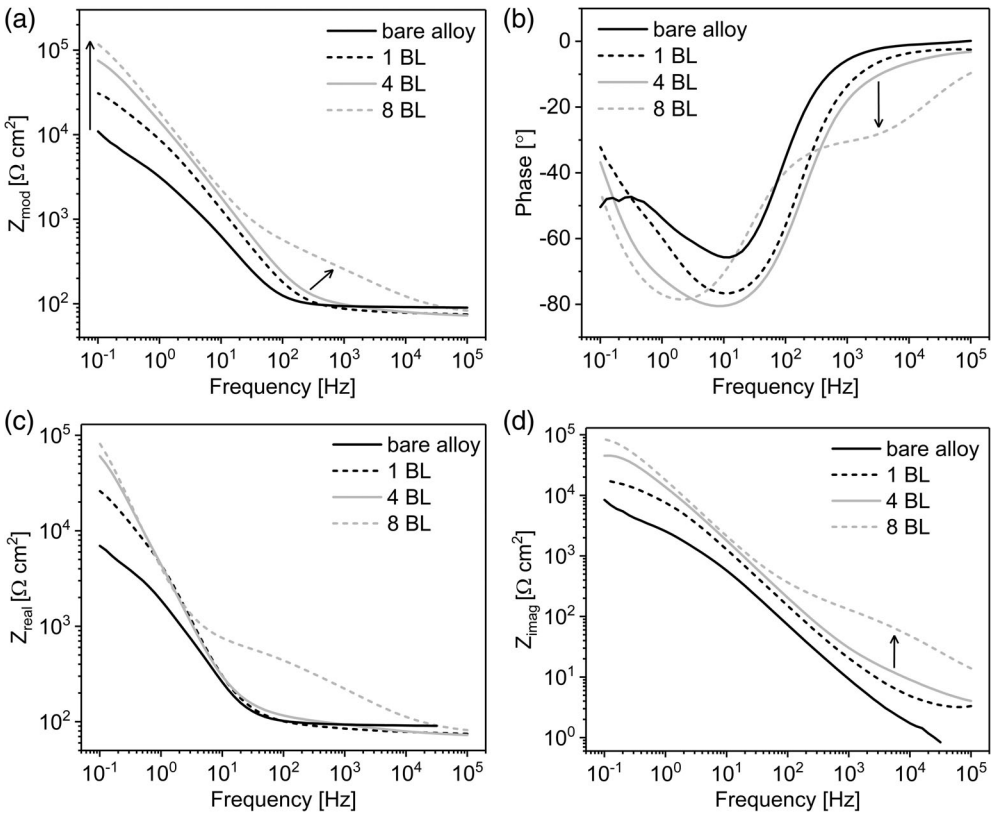

FIGURE 7 Electrochemical impedance spectroscopy plots showing the (a) overall impedance (Z_{mod}) (b) phase shift, (c) real component of the impedance (Z_{real}) and (d) imaginary component of the impedance (Z_{imag}) of AA, $(CNER/PEI)_1/AA$, $(CNER/PEI)_4/AA$ and $(CNER/PEI)_8/AA$ samples. CNER, poly([o-cresyl glycidyl ether]-co-formaldehyde); PEI, poly-(ethylenimine)

the cathodic currents was only observed with the 8 BL system.

4 | CONCLUSIONS

In this study, we demonstrate a LbL assembly of epoxy-amine BL coatings consisting of PEI and CNER on AA2024-T3 samples by means of the spin coating technique. Ellipsometry measurements of film thickness verified a proportional film growth with the number of deposited layers. However, different curing conditions proved to have a large effect on the film growth. FTIR results confirmed the requirement of a sufficient intermediate cross-linking between the layers to achieve a linear thickness increase. Potentiodynamic polarization tests indicated that the resistance to pitting corrosion was significantly improved with the increase of the coating thickness. An enhancement of the barrier properties of the coatings with increasing thickness was also confirmed by means of EIS analysis. AFM measurements revealed a smooth and homogeneous film structure. Simultaneously acquired Volta potential maps allowed the characterization of the relative nobility of IMPs present within the Al matrix under the nanometer-thin coatings. The presented multilayer coatings mimic epoxy-amine coating chemistry and allow a precise control of the film thickness, providing a suitable model system for high resolution analysis of corrosion processes at buried interfaces.

ACKNOWLEDGMENT

The authors greatly acknowledge the financial support from the PostDoc Program of the Federal Institute for Materials Research and Testing (BAM), Germany (J. Witt).

AUTHOR CONTRIBUTION

Ahed Almalla performed the experiments and analyzed the data. Andreas Hertwig and Daniel Fischer performed the ellipsometric measurements and analysis for film thickness determination. Ozlem Ozcan and Julia Witt initiated and supervised the project and wrote the manuscript with the contribution of all authors. All authors have given their approval of the final version of the manuscript.

ORCID

Julia Witt https://orcid.org/0000-0002-2733-1470

REFERENCES

[1] G. Wenjun, Y. Yingfeng, L. Xiaoyun, W. Minghai, L. Shanjun, *Colloid and Polymer Sci.* **2009**, *287*, 23.
[2] T. Hashimoto, X. Zhang, X. Zhou, P. Skeldon, S. J. Haigh, G. E. Thompson, *Corros. Sci.* **2016**, *103*, 157.
[3] R. G. Buchheit, R. P. Grant, P. F. Hlava, B. Mckenzie, G. L. Zender, *J. Electrochem. Soc.* **2019**, *144*, 2621.
[4] N. Birbilis, R. G. Buchheit, *J. Electrochem. Soc.* **2005**, *152*, B140.
[5] R. G. Buchheit, *J. Electrochem. Soc.* **1995**, *142*, 3994.
[6] N. R. Cawley, D. G. Harlow, *Mater. Sci.* **1996**, *31*, 5127.
[7] C. Blanc, B. Lavelle, G. Mankowski, *Corros. Sci.* **1997**, *39*, 495.
[8] A. Boag, R. J. Taylor, T. H. Muster, N. Goodman, D. McCulloch, C. Ryan, B. Rout, D. Jamieson, A. E. Hughes, *Corros. Sci.* **2010**, *52*, 90.
[9] A. E. Hughes, R. Parvizi, M. Forsyth, *Corros. Rev.* **2015**, *33*, 1.
[10] V. Guillaumin, P. Schmutz, G. S. Frankel, *J. Electrochem. Soc.* **2001**, *148*, B163.
[11] P. Schmutz, G. S. Frankel, *J. Electrochem. Soc.* **2019**, *145*, 2285.
[12] P. Schmutz, G. S. Frankel, *J. Electrochem. Soc.* **2019**, *145*, 2295.
[13] P. P. Leblanc, G. S. Frankel, *J. Electrochem. Soc.* **2004**, *151*, B105.
[14] C. Senöz, M. Rohwerder, *Electrochimica Acta.* **2011**, *56*, 9588.
[15] M. Rohwerder, F. Turcu, *Electrochimica Acta,* **2007**, *53*, 290.
[16] M. Rohwerder, E. Hornung, M. Stratmann, *Electrochimica Acta.* **2003**, *48*, 1235.
[17] S. S. Qureshi, Z. Zheng, M. I. Sarwar, O. Félix, G. Decher, *ACS Nano.* **2013**, *7*, 9336.
[18] M. Öhman, D. Persson, C. Leygraf, *Progress in Organic Coatings* **2006**, *57*, 78.
[19] A. Kasprzak, M. Popławska, B. Michał, O. Łabędź, I. P. Grudziński, *RSC Advances.* **2015**, *5*, 85556.
[20] G. Nikolic, S. Zlatkovic, M. Cakic, S. Cakic, C. Lacnjevac, Z. Rajic, *Sensors.* **2010**, *10*, 684.
[21] M. Sanchezsoto, P. Pages, T. Lacorte, K. Briceno, F. Carrasco, *Composites Science and Technology* **2007**, *67*, 1974.
[22] K. Wapner, M. Stratmann, G. Grundmeier, *Int. J. Adhes. Adhes.* **2008**, *28*, 59.
[23] R. Alfaro-Cuevas-Villanueva, R. Cortes-Martinez, J. J. García-Díaz, R. Galvan-Martinez, R. Torres-Sanchez, *Mater. Corros.* **2006**, *57*, 543.
[24] R. Posner, K. Wapner, M. Stratmann, G. Grundmeier, *Electrochim. Acta.* **2009**, *54*, 891.
[25] J. Xu, Q. Yang, M. S. Javed, Y. Gong, M. K. Aslam, C. Chen, *RSC Adv.* **2017**, *7*, 5880.
[26] J. A. Richardson, G. C. Wood, *Corros. Sci.* **1970**, *10*, 313.
[27] D. M. Dražić, J. P. Popić, *Appl. Electrochem.* **1999**, *29*, 43.50.
[28] H. W. Pickering, R. P. Frankenthal, *J. Electrochem. Soc.* **1972**, *119*, 1297.
[29] M. Mahdavian, M. M. Attar, *Corros. Sci.* **2006**, *48*, 4152.

How to cite this article: Almalla A, Hertwig A, Fischer D, Ozcan O, Witt J. Development of layer-by-layer assembled thin coatings on aluminium alloy AA2024-T3 for high resolution studies of local corrosion processes. *J Appl Polym Sci*. 2020; 137:e49826. https://doi.org/10.1002/app.49826